INTERNATIONAL JOURNAL OF
COASTAL, OFFSHORE & ENVIRONMENTAL ENGINEERING IJCOE Vol.9/No. 1/Winter 2024 (31-42)

Available online at: www. Ijcoe.org Manuscript Type: Original Research Article

Investigation the Surface Waves During the Indian Ocean Summer Monsoon in the Chabahar Offshore Area Using Numerical Modeling

Mohammad Pakhirehzan[1], Hossein Malakooti[1*]

[1] Faculty of Marine Sciences and Technology; University of Hormozgan, Bandar Abbas, Iran
Corresponding Author: malakooti@hormozgan.ac.ir

ARTICLE INFO

Article History:
Received: 19 Oct. 2023
Accepted: 15 Jan. 2024

Keywords:
COAWST
Indian Ocean Monsoon
MIKE SW
SWAN
WRF

ABSTRACT

Spectral and statistical analyses of wind-induced waves are very important in the design of coastal and offshore structures. In this study, the results of numerical simulations by two spectral wave models (MIKE SW and SWAN) were compared to investigate the effect of the Indian Ocean summer monsoon on wave patterns in the Chabahar offshore area in the northern Gulf of Oman. The wind field for the wave simulations was obtained by the WRF model. WRF and SWAN were implemented as wave-atmosphere subsystems of the COAWST (Coupled Ocean–Atmosphere–Wave–Sediment Transport model). For MIKE SW wind input, the output wind field of the WRF model was extracted and converted to the readable format. The results of the wave simulation are acceptable by both the COAWST and MIKE SW experiments in comparison with observational data, but the results of the COAWST model were more accurate than the results of MIKE SW in simulating wave height and period, while in simulating wave direction, MIKE SW was more accurately than COAWST. The wave spectrums were prepared for observational data and model results. All Spectrums had a single peak which means that one main frequency is responsible for the most wave energy. The best-fitted spectrum was JONSWAP for all occasions. This means that the sea state of the study area was not a fully developed sea during the simulation period. Directional wave spectrums of observational data and model results showed the south and southeast directions for the wave energy propagation.

1. Introduction

The winds over the northern Indian Ocean generally blow from the southwest during May-September (summer monsoon) and from the northeast during November–February (winter monsoon). The wind force is much stronger during the summer monsoon than during the winter monsoon [1]. Monsoons denote significant seasonal variations in winds and precipitation [2].

The ocean response to the surface severe winds is always associated with extreme wave heights, large current velocities, and substantial water level variations [3]. A fast-varying wind forms complex ocean wave fields which can propagate thousands of kilometers away from the storm center, resulting in dramatic variations of the wave field in space and time [4]. Determination of wind-induced wave conditions is a very important factor because of its impacts on economic, societal, and other human activities in coastal areas [5].

Due to the increased performance of computational resources, the use of numerical models to predict natural events is becoming more prevalent [6]. Nowadays, wave characteristics are estimated using numerical models, because of the lack of measurements in many regions [7]. Numerical simulation is among the major methods employed to study the surface wave field under the action of a tropical cyclone. The study of the surface wave field during tropical cyclones relies on the development of the wind-wave model [8]. There are many spectral wave models for wave forecast studies in the open ocean as well as in the coastal area [9]. The accuracy of the results of wave models is strongly dependent on the wind fields [10-11].

Many studies have been done to develop numerical models to study and predict environmental phenomena from a variety of temporal and spatial scales (e.g. [12-20]). In general, researchers in these studies have used three methods to implement modeling. Some have used one model (such as

WWIII, SWAN, MIKE SW, WAM, ROMS, STWAVE, etc.), some have compared the results of two models, and some have used the results of coupled models (including atmosphere, ocean, and waves models) simultaneously. The results obtained from all three methods were mostly acceptable. Of course, regarding the use of the third method (coupled models), the results are at a more favorable level than the other two methods. A set of models that can develop the interaction between the atmosphere, the ocean, and the waves will give better results. Coupled systems allow the effects of larger-scale processes to directly influence the smaller-scale response and allow sensitivity experiments to exchange prognostic variable fields between model components. Coupling of models is a sure and simple way to increase a model's complexity [6]. However, some models of the first method also give good results if correct physical components, calibration, and accurate wind field are used.

In this study, a combination of the above three methods is used. For this purpose, the simulation results in the Chabahar offshore area in the northern Gulf of Oman during the Indian Ocean summer monsoon by a coupled atmosphere-wave (SWAN [21] and WRF [22]) model as a subset of COAWST [6] have been compared with the results by the MIKE SW model [23]. The waves obtained by the COAWST are a result of the simulated wind (U_{10}, V_{10}) by the WRF applied to the simulation area by SWAN, and this wind, in turn, is affected by the roughness coefficient, which determines by the wave height and wavelength sent from the SWAN to the WRF. The SWAN model can be run individually, but researchers who have used coupled model have claimed that coupling is more accurate than individual execution in addition to saving time ([6, 24-28]). Also, the waves obtained by MIKE SW are the result of simulated wind (U_{10}, V_{10}) which are extracted from the results of the WRF model and converted into a format that can be read by the MIKE SW model.

The WRF model is designed and presented for numerical simulation of the atmosphere. The WRF supports several dynamical and physical parameterizations that allow for the various configurations, tailored to atmospheric studies [22]. The SWAN and the MIKE SW are known as two widely used, well-tested spectral wave models for near-shore simulations. Both models represent the generation, propagation, and dissipation of waves and include the effects of refraction and shoaling on wave propagation, accounting for wave dissipation by white-capping, wave-wave interactions, bottom friction, and depth-induced wave breaking [29]. The SWAN model is presented for use in an enclosed sea, although it was initially designed primarily for use in coastal environments [30]. The MIKE SW model is based on a flexible mesh, which allows for coarse spatial resolution in the offshore area and high resolution in the shallow coastal waters [31].

SWAN can be run on both structured and unstructured grids, its spatial discretization is based on a vertex-centered method, and the control volume in SWAN is a polygon, while MIKE SW only uses unstructured grids, its spatial discretization is a cell-centered method, and the control volume in MIKE SW is triangular. The major difference between the numerical methods is that the SWAN uses fully implicit method time integration whereas MIKE SW is an explicit approach [23, 32, 33].

Comparison of wave simulation results by different models has been studied by various authors. Strauss et al. [34] presented comparative simulations by SWAN and MIKE SW in the Gold Coast of Australia. They claimed that model simulations are compared with observed data from existing wave recording buoys. Their results showed that the inclusion of wind in the modeling undertaken did not improve the model's accuracy and winds over 10 m/s led to an overestimation of significant wave height while increasing the processing time. Moeini and Etemad-Shahidi [7] compared the results of wave parameters simulation by SWAN and MIKE SW for Lake Erie in the United States. They used a field data set of Lake Erie for testing the performance of the simulations. They claimed that the average scatter index of SWAN was about 16% for significant wave height and 19% for peak wave period; while the average scatter index of MIKE SW was calculated about 20% and 13% for significant wave height and peak wave period, respectively. Both models were also evaluated for the prediction of wave direction and it was found that MIKE SW results are slightly more accurate than those of SWAN. Montoya et al. [35] performed a comparison between WAVEWATCH III and SWAN, using data from Hurricane Katrina in the Gulf of Mexico. They simulated sea surface directional wave spectrum and other wave parameters and their relation with the drag coefficient. They compared simulated data with in-situ buoy data. Their results showed that the WAVEWATCH III presented the best statistical comparisons for the main wave parameters, such as significant wave height and peak wave period, and the SWAN model tends to overestimate the maximum values for significant wave height for some buoys and the peak wave period for almost all the buoys. Fonseca et al. [36] presented results of wave characteristics simulation in shallow waters by MIKE SW, SWAN, and STWAVE models in the Portuguese coasts. In situ measurements from buoys and Acoustic Doppler Current Profilers (ADCP) were used to validate the model simulations. The researchers claimed that, both MIKE SW and SWAN are complex models and have a large set of formulations and parameter choices, and STWAVE produced good

results and is considerably faster than the other models.

This study is structured as follows. The study area is presented in the next section. Numerical model definitions including estimation and the governing equations of them, a brief outline of the SWAN, MIKE SW, and WRF models, Setup, calibration, and Validation of models, and a definition of wave spectrum and its application are introduced in the section 3. The main wind and wave simulated parameters by models, the directional and frequency wave spectrum, and their comprehensive comparison are presented in section 4. Finally, the conclusions and recommendations are presented in section 5.

2. Study Area

The study area is located in the northern Gulf of Oman and southeast of Iran in the offshore area of Chabahar port (Figure 1). The Chabahar port is the only ocean port in Iran. This port is a gateway for Central Asian countries to expand their trade first with the Indian Ocean countries and then with the rest of the world. The Chabahar port lies at the mouth of the Chabahar Bay and is always exposed to high waves, resulting from cyclones and monsoons coming from the Indian Ocean. The area under investigation for wave characteristics analysis is located between latitudes 24°40' to 25°40' N, and longitudes 60° to 61° E.

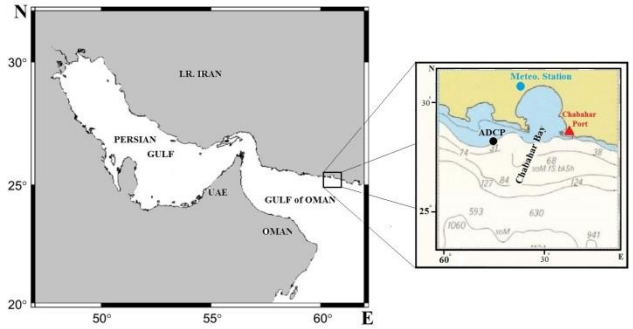

Figure 1. Area under investigation

3. Material and Methods

3.1 Numerical Models Definitions

The coupled atmosphere–wave modeling system includes WRF, SWAN, and the Model Coupling Toolkit [37] to exchange data fields between the wave and the atmosphere model. The Model Coupling Toolkit (MCT) allows the transformation of various distributed data between component models using a parallel coupled approach. MCT is a program written in Fortran90 and works with the MPI communication protocol. It is compiled as a set of libraries, which are linked during the compilation [6]. Fields exchanged in the coupled system are shown in Figure 2. The WRF model transfers wind speeds at 10 meters above the sea surface (U_{10}, V_{10}) to SWAN, and SWAN passes back significant wave height, wavelength, and wave period [26].

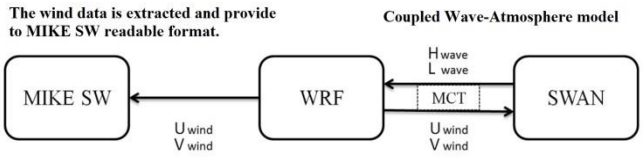

Figure 2. Data fields exchanged between models

3.2 WRF Model

The WRF is a non-hydrostatic, quasi-compressible atmospheric model with several boundary layer schemes, as well as both explicit and parameterized physics [13]. WRF is an advanced mesoscale numerical weather prediction system designed to serve both operational forecasting and atmospheric research needs [38]. The time integration scheme in the model uses the third-order Runge-Kutta scheme, and the spatial discretization employs second to sixth-order schemes [39]. The WRF model has two large classes of simulations that can produce both ideal and real data simulations. In the simulation with real data, a pre-processing system named WPS is required to generate all atmospheric fields and static geographical data for initial boundaries. The work of vertically interpolating meteorological fields to WRF eta levels is performed within the real program [22].

The WRF should be provided by physical schemes which are to be fitted with the season and the geographical area. Based on recent sensitive studies in low-level wind simulation, three important physical schemas of Land Surface Model (LSM), Surface Layer (SL), and planetary boundary Layer (PBL) have been introduced [40-43]. To modify the WRF code to provide an enhanced bottom roughness when computing the bottom stress over the ocean, Warner et al. [12] have recommended the use of Mellor-Yamada Nakanishi Niino (MYNN) scheme for PBL. This scheme solves higher-order Turbulent Kinetic Energy equations than the other schemes (e.g. MYJ scheme by Janjic [44], and YSU scheme by Hong et al. [45]). The equation of the MYNN PBL scheme is affected by the surface stress directly. In the MYNN scheme, the default surface roughness (z_0) method is as follows by Fairall et al. [46], in which the Charnock parameter (c_a) is a function of 10 m wind speed (U_{10}):

$$z_0 = \frac{c_a U_*^2}{g} + \frac{v}{U_*} \quad (1)$$

$$c_a = \begin{cases} 0.011, U_{10} \le 10 ms^{-1} \\ \frac{1}{8}(7U_{10} + 18) \times 10^{-3}, 10 ms^{-1} < U_{10} < 18 ms^{-1} \\ 0.018, U_{10} \ge 18 ms^{-1} \end{cases} \quad (2)$$

Here, u_* is the surface stress (friction velocity), g is gravity, and v is the viscosity. After the WRF code has been modified to allow the MYNN scheme to incorporate the effect of the waves according to the formula of Taylor and Yelland [47], the roughness length equation is as follows:

$$z_0 = 1200\, H_s \left(\frac{H_s}{L_p}\right)^{4.5} + 0.11 \frac{v}{U_*} \quad (3)$$

Here, H_s is the significant wave height, and L_p is the mean wavelength. This option is activated when coupling to the wave model and was chosen as a representative method [6, 48].

3.3 SWAN Model

The SWAN resolves the spectral balance equation in the Cartesian system or spherical coordinates as a function of action density spectrum N(x,t,σ,θ). SWAN can simulate shoaling due to spatial variations at the bottom. It can also simulate refraction, bottom friction, depth-induced wave breaking, and the three-wave interactions, which are very important factors for shallow waters [35]. SWAN solves the action balance equation as follows:

$$\frac{\partial \mathrm{N}}{\partial \mathrm{t}}+\frac{\partial \mathrm{c_x N}}{\partial \mathrm{x}}+\frac{\partial \mathrm{c_y N}}{\partial \mathrm{y}}+\frac{\partial \mathrm{c_\theta N}}{\partial \theta}+\frac{\partial \mathrm{c_\sigma N}}{\partial \sigma}=\frac{\mathrm{S}_{(\sigma,\theta)}}{\sigma} \quad (4)$$

Where N is the action density spectrum. The first term on the left-hand side represents the local rate of change of action density in time, the second and third terms represent the propagation of action density in geographic space, and the fourth term represents depth-induced and current-induced refraction. The fifth term represents the shifting of the relative frequency due to variations in depth and currents. The term $S(\sigma,\theta)$ is the source term in terms of energy density [49].

SWAN contains several physical processes that add or withdraw wave energy to or from the wave field. The processes included are wind input, white-capping, bottom friction, depth-induced wave breaking, obstacle transmission, nonlinear wave-wave interactions (quadruplets and triads), and wave-induced set-up [32].

One of the most important calibration factors in SWAN is the changing rate of energy dissipation by the white-capping. For this purpose, the quasi-linear model by Hasselmann [50], and Janssen [51] are considered. The white-capping formulation implemented in SWAN is:

$$\mathrm{S_{dis}}=-\mathrm{C_{ds}}\left[(1-\delta)+\delta\left(\frac{\mathrm{k}}{\bar{\mathrm{k}}}\right)\right]\frac{\mathrm{k}}{\bar{\mathrm{k}}}\left(\frac{\tilde{\mathrm{S}}}{\tilde{\mathrm{S}}_{\mathrm{PM}}}\right)^{\mathrm{q}}\tilde{\sigma}\,\mathrm{E}(\sigma,\theta \quad (5)$$

$$\begin{cases}\mathrm{C_{ds}}=2.36\times10^{-5},\delta=0.8 & \text{for Komen et al. [52]}\\ \mathrm{C_{ds}}=4.10\times10^{-5},\delta=0.5 & \text{for Janssen [51]}\end{cases} \quad (6)$$

Here, k is the wave number, $\tilde{k}$ mean spectral wave number and $\tilde{\sigma}$ are the mean spectral wave frequency. The quantity $\tilde{S}$ is the mean spectral steepness, and $\tilde{S}_{PM}=\sqrt{3.02\times10^{-3}}$ is the mean steepness of the Pierson-Moskowitz spectrum. Coefficient for determining the rate of white-capping dissipation (C_{ds}), and coefficient which determines the dependency of the white-capping on wave number (δ) are the tuning parameters in the equation [11].

The bottom friction in SWAN is a combination of the empirical model of JONSWAP [53], the drag law model of Collins [54], and the eddy-viscosity model of Madsen et al. [55]:

$$\mathrm{S_{ds,b}}=-\mathrm{C_b}\frac{\sigma^2}{\mathrm{g^2\sinh^2\kappa d}}\mathrm{E}(\sigma,\theta) \quad (7)$$

Here, C_b is a bottom friction coefficient [32].

3.4 MIKE SW Model

The MIKE SW simulates the growth, decay, and transformation of wind-generated waves and swells in offshore and coastal areas. The waves in this module are represented by the density spectrum $N(\sigma, \theta)$. The independent parameters are the relative angular frequency ($\sigma=2\pi f$), and the direction of wave propagation (θ). The governing equation is the wave action balance equation formulated in either Cartesian or spherical coordinates [56]:

$$\frac{\partial \mathrm{N}}{\partial \mathrm{t}}+\nabla.(\vec{\mathrm{v}}\,\mathrm{N})=\frac{\mathrm{s}}{\sigma}\rightarrow\frac{\partial}{\partial \mathrm{t}}\mathrm{N}+\frac{\partial}{\partial \mathrm{x}}\mathrm{C_x N}+\frac{\partial}{\partial \mathrm{y}}\mathrm{C_y N}+\frac{\partial}{\partial \sigma}\mathrm{C_\sigma N}+\frac{\partial}{\partial \theta}\mathrm{C_\theta N}=\frac{\mathrm{s}}{\sigma} \quad (8)$$

where N is wave action density, σ is the relative angular frequency, θ is the wave direction, C_x, C_y, C_σ, C_θ are celerity characteristics in a geographical and spectral coordinate system, and S is the energy source term, which represents the superposition of source function describing various physical phenomenon .

$$\mathrm{S}=\mathrm{S_{in}}+\mathrm{S_{nl}}+\mathrm{S_{ds}}+\mathrm{S_{bot}}+\mathrm{S_{surf}} \quad (9)$$

Where S_{in} represents the generated energy by the wind, S_{nl} is the wave energy transfer due to non-linear wave-wave interaction, S_{ds} is the dissipation of wave energy due to white capping, S_{bot} is the dissipation due to bottom friction and S_{surf} is the dissipation of wave energy due to depth-induced breaking [57-58].

The two main factors for model calibration in MIKE SW are white-capping and bottom friction. The white-capping is provided by Janssen [51] in terms of wave number:

$$\mathrm{S_{ds}}(\mathrm{f},\theta)=-\mathrm{C_{ds}^*}\left[\frac{\bar{\alpha}}{\bar{\alpha}_{\mathrm{PM}}}\right]^{\mathrm{m}}\left\{(1-\delta)\frac{\mathrm{k}}{\bar{\mathrm{k}}}+\delta\left(\frac{\mathrm{k}}{\bar{\mathrm{k}}}\right)^2\right\}\bar{\sigma}\mathrm{E}(\mathrm{f},\theta) \quad (10)$$

Here, $\bar{\alpha}$ is the overall steepness of the wave field, $\bar{\alpha}_{PM}$ is the value of $\bar{\alpha}$ for the Pierson-Moskowitz spectrum, $\bar{\mathrm{k}}$ is the mean wave number, and $\bar{\sigma}$ is the mean relative angular frequency. C_{ds}, δ, and m are constant and the default values for them are 4.5, 0.5 and 4 respectively [23]. The rate of dissipation due to bottom friction by Komen et al. [52] is:

$$\mathrm{S_{bot}}(\mathrm{f},\theta)=-\left(\mathrm{C_f}+\frac{\mathrm{f_c}(\bar{\mathrm{u}},\bar{\mathrm{k}})}{\mathrm{k}}\right)\frac{\mathrm{k}}{\sinh 2\mathrm{kd}}\mathrm{E}(\mathrm{f},\theta) \quad (11)$$

Here, C_f is a friction coefficient with a typical value between 0.001 to 0.01 m/s depending on the bed and flow conditions. The default value for C_f is 0.0077 m/s. the k is the wave number, d is water depth, f_c is the friction coefficient for current with zero as the default value corresponding to excluding the effect of the current on the bottom friction, and u is the current velocity [23].

3.5 Models Setup and Validation

Initially, to make the results of the simulations closer to the real data, the models must be validated. The validation period is considered from July 3 to 6, 2016.

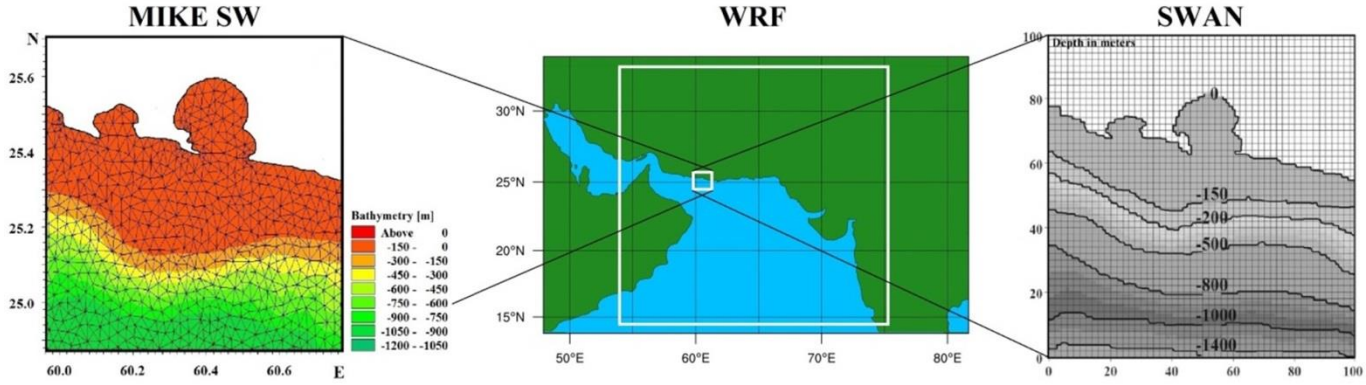

Figure 3. Telescopic domains configuration of WRF and wave models (MIKE SW & SWAN) domains.

The recorded wind data at Chabahar meteorological station with 3 hours time interval at 25°26' N and 60°22' E, prepared by Iran Meteorological Organization, and the recorded wave data by ADCP (Acoustic Doppler Current Profilers) with one hours time interval at 25°13' N and 60°16' E, prepared by Iranian Port and Maritime Organization, which located in 24 km southeast of the mouth of Chabahar Bay, were used to calibrate and validate the models.

The best configuration for the atmospheric model (WRF) was selected based on previous studies [40-42, 59-60]. Two telescopic domains were designated. The external domain (Nx × Ny: 80×80) with 27 km resolution, and the internal domain (Nx × Ny: 13×13) with 9 km resolution covers the Chabahar Bay and offshore area, which exactly matches the domain of wave models (Figure 3).

The microphysics options applied in this study include the WRF Single-Moment 6-class scheme by Hong et al. [61], long wave radiation (RRTM) by Mlawer [62], and short wave radiation by Dudhia [63], the MYNN planetary boundary layer (PBL) scheme by Nakanishi and Niino [64], and the Noah Land Surface Model (LSM) by Chen and Dudhia [65]. Initial and boundary conditions for WRF are prepared by FNL data type. The NCEP FNL (Final) Operational Global Analysis data are on a 1° by 1° grid prepared operationally every six hours. This product is received from the Global Data Assimilation System (GDAS), which continuously collects observational data from the Global Telecommunications System (GTS), and other sources, for many analyses. The analyses are available on the surface, at 26 levels from 1000 to 10 mb, in the surface boundary layer and at some sigma layers, the tropopause, and a few others.

The computational grid for SWAN was prepared as a regular mesh with several 100×100 grids was considered. The length and width of each cell are about 1.8 km. The SWAN model origin of the grid is at 24° 50' N and 60° 0.0' E, and the resolution in the geographical space is 0.016 × 0.016 degrees (Figure 3). The mode of implementation is two-dimensional and non-stationary, the spectral resolution varying from 0.042 Hz to 0.65 Hz with a $\sigma m+1=1.1\sigma m$ distribution, the number of frequencies in the spectral space is 24, and the number of directions in the spectral space is 36, and the coordinates is spherical.

For calibration of the SWAN model, the white-capping was considered. For the rate of energy dissipation by white-capping (C_{ds}), at first, the model default value (2.36×10^{-5}) was considered. The calculation was done in a non-stationary method with a time step of 30 minutes. The results show that the observational wave height data were above the simulated wave height. By decreasing the value of the white-capping, finally, the best agreement was obtained with the value of 1.00×10^{-6}. For energy dissipation due to depth breaking, the value of the energy dissipation coefficient and the ratio of maximum wave height on depth were considered 0.8 and 0.01, respectively.

The coupled wave-atmosphere model was executed with SWAN and WRF. The time step of WRF and SWAN is adjusted equal to 180 seconds and 30 minutes increment, respectively. The two models were synchronized 1800 seconds to exchange data fields through the MCT coupler during the simulation. Figure 4 represents the synoptic pattern of the area with maximum wind speed and wind field at 10 m level, and the pattern of sea level pressure distribution over the area. Figure 5 shows the time series of wind and wave parameters simulated by COAWST in comparison with observational data.

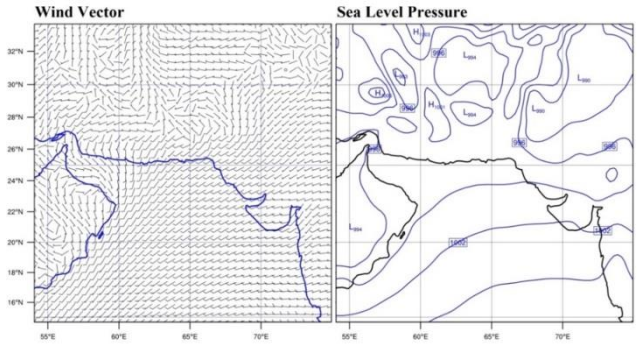

Figure 4. Synoptic pattern of 10 m wind field (left) and sea level pressure distribution (right) at annual maximum wind speed (2016 July 05, 12:00).

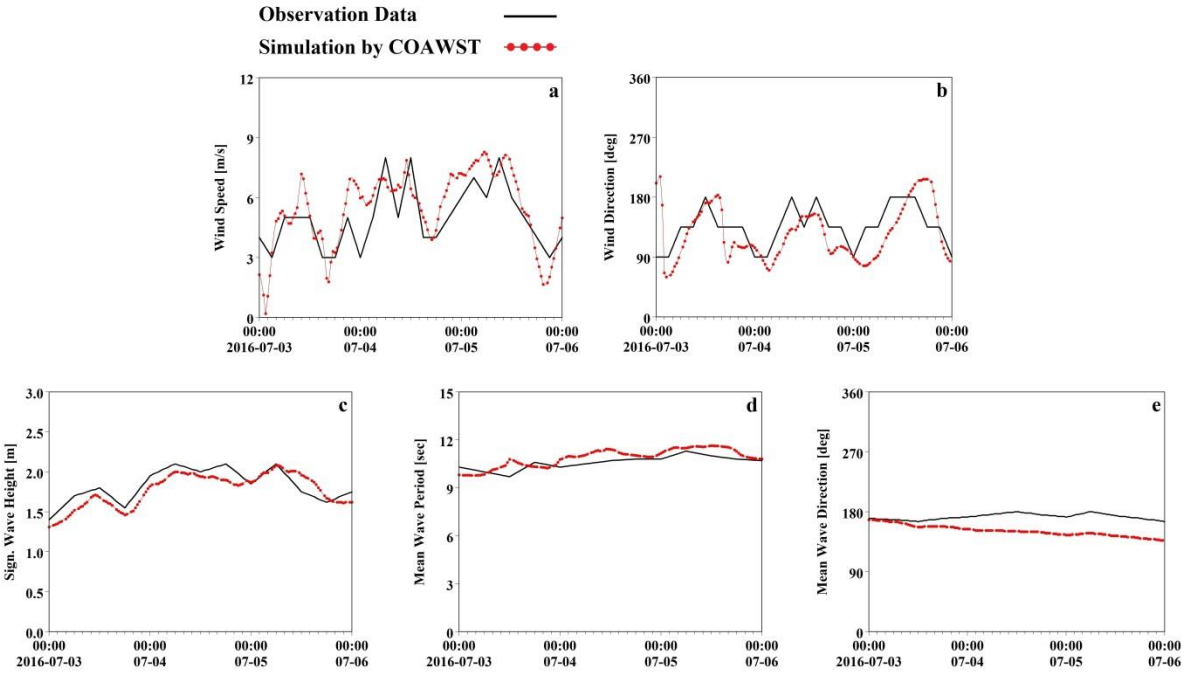

Figure 5. Time series of (a) wind speed, (b) wind direction, (c) Sign. Wave Height, (d) Mean wave Period and (e) Mean Wave Direction derived from COAWST in comparison with observational data during the validation period.

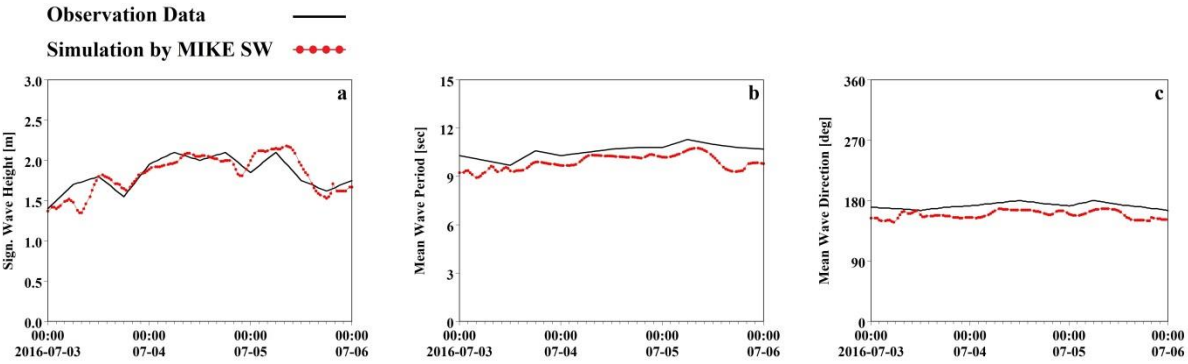

Figure 6. Time series of (a) Sign. Wave Height, (b) Mean wave Period, and (c) Mean Wave Direction derived from MIKE-SW in comparison with observational data during the validation period

The MIKE SW has been adapted to simulate the wave parameters in the validation period (July 3 to 6, 2016). The flexible mesh has been adapted for the domain of simulation. This mesh has been generated with the 3663 cells (Figure 3). The hourly wind speed and direction adapted to the MIKE SW model were derived from the WRF simulations. After the WRF is implemented in the coupled system, the wind data is extracted and provided to MIKE SW in a readable format. The modeled area is bordered by three open boundaries at the west, east, and south, and one land boundary at the north. For the open boundary conditions, the water level elevation was considered at all three open boundaries. Considering the geographical location of the area, and taking into account the selected period for simulation, the water temperature was set to 25°, and the water salinity was set to 35 ppt. Figure 6 shows time series of wave parameters simulated by MIKE SW in comparison with observational data.

For accuracy evaluation of the simulation results, the Bias parameter, Correlation Coefficient (CC), Root Mean Square Error (RMSE), and Scattering Index (SI) were considered [66] and represents in Table 1.

$$\text{Bias} = \sum_{i=1}^{N} \frac{1}{N} (y_i - x_i) \quad (12)$$

$$\text{CC} = \sum(x_i - \bar{x})(y_i - \bar{y}) / \sqrt{\sum(x_i - \bar{x})^2 \sum(y_i - \bar{y})^2} \quad (13)$$

$$\text{RMSE} = \sqrt{1/N \sum_{i=1}^{N} (y_i - x_i)^2} \quad (14)$$

$$\text{SI} = \sqrt{\frac{1}{N}\sum_{i=1}^{N} (y_i - x_i)^2} \Big/ \frac{1}{N}\sum_{i=1}^{N} x_i \quad (15)$$

Table 1. Performance evaluation of wave parameters base on computational errors during validation period.

MODEL	Parameters	Bias	CC	RMSE	SI
COAWST	Wind Sp.	0.47	0.78	1.24	0.24
	Wind Dir.	-1.28	0.52	6.50	0.26
	Wave Height	0.13	0.74	0.19	0.10
	Wave Period	-1.01	0.90	1.08	0.10
	Wave Dir.	-4.87	0.91	8.25	0.16
MIKE SW	Wave Height	0.19	0.73	0.32	0.17
	Wave Period	-1.98	0.45	3.20	0.30
	Wave Dir.	-7.60	0.41	8.69	0.16

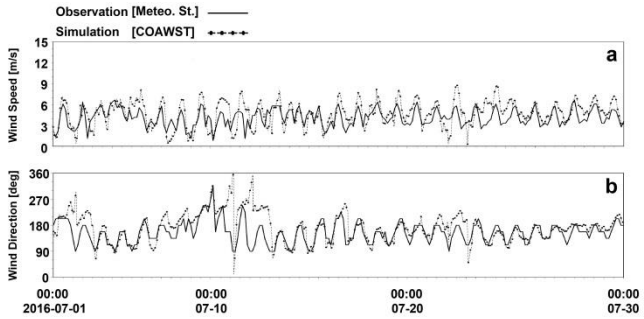

Figure 7. (a) Wind speed, and (b) wind direction simulated by COAWST (by WRF) in comparison with observational data

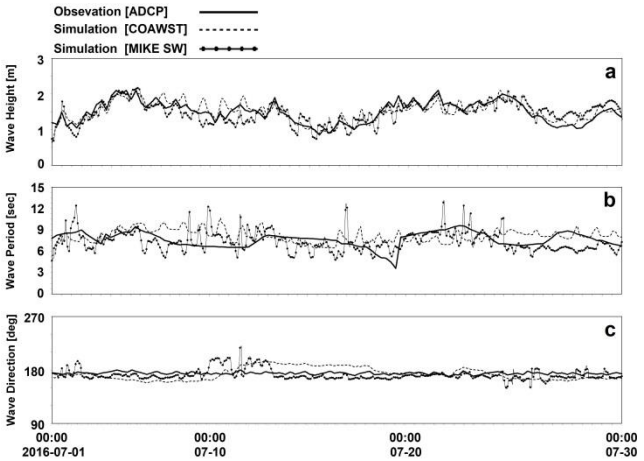

Figure 8. Time series of (a) Sign. Wave Height, (b) Mean wave Period, and (c) Mean Wave Direction derived from COAWST and MIKE SW in comparison with observational data

Table 2. Computational errors for simulated parameters in comparison with observational data in July, 2016.

MODEL	Parameters	Bias	CC	RMSE	SI
COAWST	Wave Height	0.22	0.90	0.15	0.10
	Wave Period	0.46	0.61	0.98	0.10
	Wave Dir.	7.50	0.66	2.97	0.12
MIKE SW	Wave Height	0.24	0.83	0.20	0.13
	Wave Period	0.66	0.78	3.11	0.31
	Wave Dir.	12.76	0.49	9.68	0.12

4. Results and Discussions

Figures 7 and 8 represent the time series data derived from the model results at the monitoring point. Figure 7 contains wind speed and direction for the July of 2016, during the summer monsoon of the Indian Ocean. Since Chabahar offshore is further away from the monsoon area, the intensity of the wind seems justified. The maximum wind speed reached up 10 m/s at its maximum and the wind direction was mainly from the south.

Figure 8a shows the significant wave height and contain two points. First, there is high coordination between the model's results and the observational data. Second, based on past experiences and due to the intensity of the wind, the significant wave height is higher than expected, and as a result, indicating the effect of swell waves. According to the diagrams, the height of the wave in July is between 0.85 m to 2 m and the average is 1.5 m.

Figure 8b shows the mean wave period, which shows that the results of the models are not desirable, compared to the observed data but are acceptable. Figure 8c shows the mean wave direction results by models compared with the real data that are in good agreement with the wind direction. The wave direction is mainly from the south. Table 2 represents the computational errors for simulated parameters by models compared with real data in July, 2016.

The scatter plots are presented in Figure 9. By analyzing Figures 8 and 9 and Table 2, it can be concluded that the results of the simulations by both models are accurate and acceptable, but the results of the COAWST model are in better agreement with the real data than the results of MIKE SW model.

To calculate and plot the wave spectrum, a time interval on July 3 to 7, 2016 was considered. This time interval included maximum wind speed during July 2016. For this purpose, significant wave height, frequency, peak angular frequency, peak wave period, and maximum wave height are needed (Table 3). The Wave spectrums were prepared for COAWST, MIKE SW, and ADCP data. The smoothing Spline technique from MatLab software was used. To distinguish which of the presumed wave spectrums could better represent the pattern of waves in the Chabahar offshore area, the JONSWAP spectrum, Bretschneider spectrum, and Ochi spectrum were considered.

According to Figure 10, the best-fitted pattern for the concerning point is represented by the JONSWAP spectrum. The frequency spectrum of waves shows a single peak type spectrum, which suggests that just one main frequency (period) is responsible for the generated waves. The peak value of observational (ADCP) data is located at 4.56 m^2s in frequency of 0.09 Hz, while by MIKE SW this value is 4.65 m^2s in frequency of 0.12 Hz, and by COAWST is 4.55 m^2s in frequency of 0.08 Hz. According to the results, the peaks of the wave spectrums diagrams are almost on the same level. Also, the smoothed and unsmoothed spectrum of the COAWST model has a better agreement with the spectrum of observational data.

Figure 11 shows the directional wave spectrum by ADCP, MIKE SW, and COAWST. According to diagrams, the direction of wave propagation has oriented from south and southeast and is affected by wind direction. The MIKE SW wave propagation was located closer to ADCP wave propagation than COAWST.

Table 3. Wave parameters at maximum wind speed during July, 2016.

Date & Time	Observation or Model	Tp (sec)	Fp (Hz)	WD (deg)	Hmax (m)	Hs (m)	Max. of Spectrums (m^2.s)			
							S(f)	JONSWAP	Ochi	Bretschneider
2016-07-05 06:00	ADCP	11.1	0.09	180	2.10	1.55	4.56	4.89	2.38	2.01
	MIKE SW	8.33	0.12	165	2.18	1.75	4.65	4.66	2.79	2.09
	COAWST	12.5	0.08	149	2.08	1.50	4.55	4.70	2.33	1.69

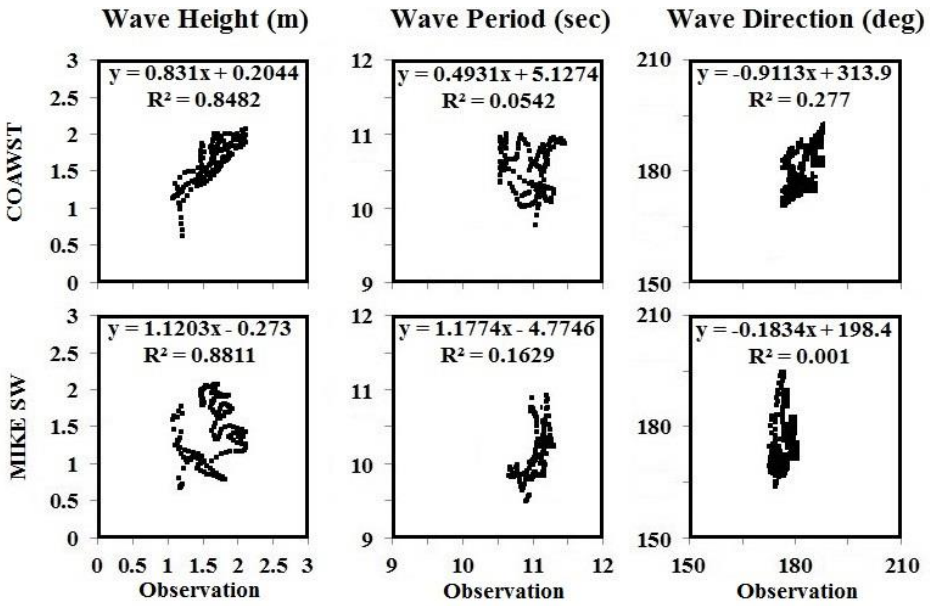

Figure 9. Scatter plot diagram for wave height, wave period, and wave direction.

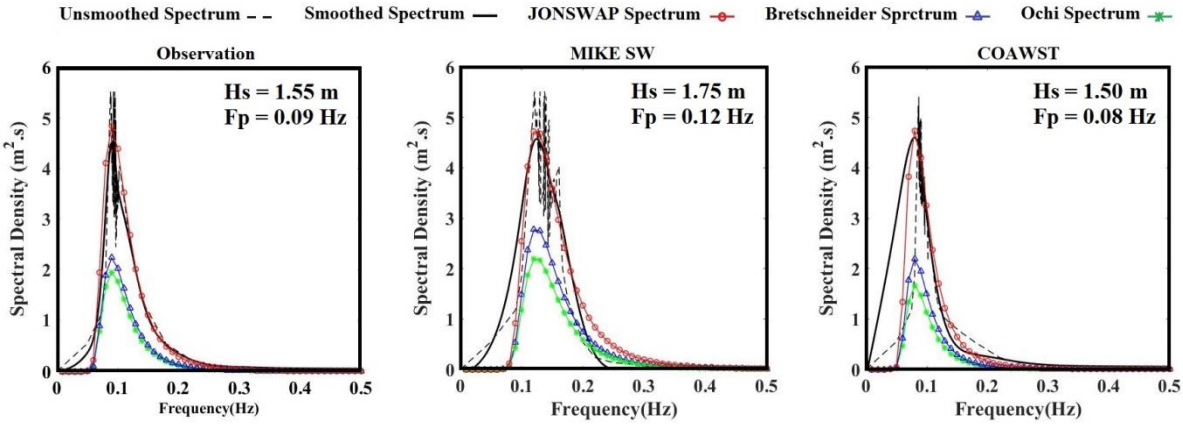

Figure 10. Frequency wave spectrums for Observation (left), MIKE SW (mid), and COAWST (right) simulations results for period of maximum wind speed in July, 2016.

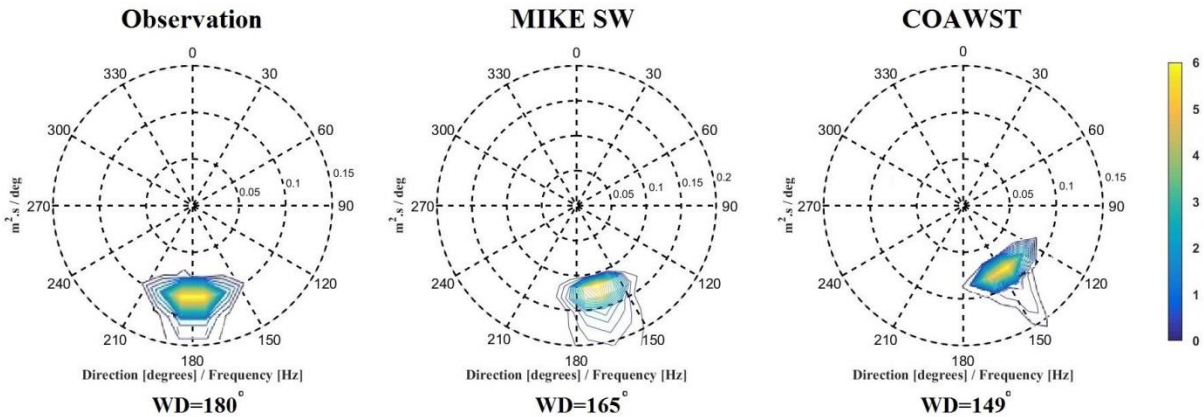

Figure 11. Directional wave spectrums for ADCP (left), MIKE SW (mid), and COAWST (right) simulations results for the period of maximum wind speed in July 2016.

5. Conclusion

In this study, a comparison between SWAN and MIKE SW wave models for the wave field in the Chabahar offshore area in the northern Gulf of Oman was implemented during the peak activity of the Indian Ocean Summer Monsoon occurs in July 2016. Wind conditions for the wave models were obtained by the WRF model in two ways. First, WRF and SWAN were implemented as wave-atmosphere subsystems of the COAWST (Coupled Ocean–Atmosphere–Wave–Sediment Transport) model. Second, the wind field of the WRF model output was extracted and converted to the MIKE SW readable format.

Simulated wind parameters including speed and direction are compared with observational data from the Chabahar meteorology station. The result of the wind simulation was acceptable by COAWST and was found closer to the observational data according to the computational errors. The results of the wave simulation are acceptable by both the COAWST and MIKE SW experiments in comparison with observational data of ADCP (Acoustic Doppler Current Profilers), but the results of the COAWST were found closer to the observational data. The results of the COAWST model were more accurate than the results of MIKE SW in simulating wave height and period, while in simulating wave direction, MIKE SW was more accurate than COAWST.

The wave spectrums were prepared for observational data and models results during the interval of maximum wind speed in July 2016. All Spectrums had a single peak which means that one main frequency is responsible for the most wave energy. Provided spectrums were compared with standard spectrums of JONSWAP, Bretschneider, and Ochi. The best-fitted spectrum was JONSWAP for all occasions. This means that the sea state of the Chabahar offshore area was not a fully developed sea during the simulation period. The peak of the frequency spectrum diagram for the COAWST model is closer to the frequency spectrum of observational data than to the MIKE SW.

Directional wave spectrums of observational data and models results showed the south and southeast directions for the wave energy propagation. The direction of wave propagation is affected by wind direction. The MIKE SW wave propagation was found closer to observational wave data propagation than COAWST.

As a general conclusion, it can be stated that both models have provided acceptable results. It might be expected that the results of the COAWST model match the observational data to a higher degree than the results of the MIKE SW model, but in practice, this is not the case. The complexity of a set is not always the reason for its better results. Although MIKE SW model is a complete but simple set, it provides acceptable results compared to the complex COAWST set, which is the result of the efforts of J.C. Warner and his colleagues. Perhaps the difference in the views of physical oceanographers in the Netherlands and Denmark in the DELFT and DHI collections for the production of SWAN and MIKE models, respectively, according to the results of this research, will finally end in the same conclusion.

Of course, the extent of the simulation area and wind field condition induced by monsoons or cyclones can also be decisive in the obtained results. One should wait for another research with the same conditions but with a larger simulation scope in other ocean locations, and with different wind fields !

Acknowledgment

The authors are thankful to Iranian Meteorological Organization and Iranian Port and Maritime Organization for providing observational data.

6. References

[1] Shankar, D., Vinayachandran, P.N. and Unnikrishnan, A.S, (2002). *The monsoon currents in the north Indian Ocean. Progress in oceanography,* 52(1), p.63-120.

[2] Zheng, C., Pan, J., Tan, Y., Gao, Z., Rui, Z. and Chen, C., (2015). *The seasonal variations in the significant wave height and sea surface wind speed of the China's seas. Acta Oceanologica Sinica,* 34, p.58-64.

[3] Allahdadi, M.N., Chaichitehrani, N., Allahyar, M. and McGee, L., (2017). *Wave spectral patterns during a historical cyclone: a numerical model for cyclone Gonu in the northern Oman Sea. Open Journal of Fluid Dynamics,* 7(2). P.131-151.

[4] Zhou, L.M., Wang, A.F. and Guo, P.F., (2008). *Numerical simulation of sea surface directional wave spectra under typhoon wind forcing. Journal of Hydrodynamics, Ser. B,* 20(6), p.776-783.

[5] Kutupoğlu, V., Çakmak, R.E., Akpınar, A. and van Vledder, G.P., (2018). *Setup and evaluation of a SWAN wind wave model for the Sea of Marmara. Ocean Engineering,* 165, p.450-464.

[6] Warner, J.C., Armstrong, B., He, R. and Zambon, J.B., (2010). *Development of a coupled ocean–atmosphere wave sediment transport (COAWST) modeling system. Ocean modeling,* 35(3), p.230-244.

[7] Moeini, M.H. and Etemad-Shahidi, A., (2007). *Application of two numerical models for wave hindcasting in Lake Erie. Applied Ocean Research,* 29(3), p.137-145.

[8] Xu, F., Cheng, Z. and Xia, M., (2020). *Surface wave field under binary typhoons Sarika and Haima (2016) in South China Sea. Estuarine, Coastal and Shelf Science,* 241, p.106802.

[9] Abdollahzadehmoradi, Y., Erdik, T., Özger, M. and Altunkaynak, A., (2014). *October. Application of MIKE 21 SW for wave hindcasting in Marmara Sea Basin for the year 2012. In 11th international congress on advances in civil engineering (ACE)*, p.21-25.

[10] Ardhuin, F., Bertotti, L., Bidlot, J.R., Cavaleri, L., Filipetto, V., Lefevre, J.M. and Wittmann, P., (2007). *Comparison of wind and wave measurements and models in the Western Mediterranean Sea. Ocean Engineering*, 34(3-4), p.526-541.

[11] Rusu, L., Bernardino, M. and Guedes Soares, C., (2014). *Wind and wave modelling in the Black Sea. Journal of Operational Oceanography*, 7(1), p.5-20.

[12] Warner, J.C., Sherwood, C.R., Signell, R.P., Harris, C.K. and Arango, H.G., (2008). *Development of a three-dimensional, regional, coupled wave, current, and sediment-transport model. Computers & geosciences*, 34(10), p.1284-1306.

[13] Zambon, J.B., He, R. and Warner, J.C., (2014). *Investigation of hurricane Ivan using the coupled ocean atmosphere wave sediment transport (COAWST) model. Ocean Dynamics*, 64, p.535-1554.

[14] Anton, I.A., Rusu, L. and Anton, C., (2019). *Nearshore wave dynamics at Mangalia beach simulated by spectral models. Journal of Marine Science and Engineering*, 7(7), p.206.

[15] Liang, B., Gao, H. and Shao, Z., (2019). *Characteristics of global waves based on the third-generation wave model SWAN. Marine Structures*, 64, p.35-53.

[16] Pradhan, U.K., Mishra, P., Mohanty, P.K., Panda, U.S. and Ramanamurthy, M.V., (202). *Modeling of tidal circulation and sediment transport near tropical estuary, east coast of India. Regional Studies in Marine Science*, 37, p.101351.

[17] Son, B. and Do, K., (2021). *Optimization of SWAN wave model to improve the accuracy of winter storm wave prediction in the East Sea. Journal of Ocean Engineering and Technology*, 35(4), p.273-286.

[18] Islek, F. and Yuksel, Y., (2021). *Inter-comparison of long-term wave power potential in the Black Sea based on the SWAN wave model forced with two different wind fields. Dynamics of Atmospheres and Oceans*, 93, p.101192.

[19] Li, Z., Tam, C.Y., Li, Y., Lau, N.C., Chen, J., Chan, S.T., Dickson Lau, D.S. and Huang, Y., (2022). *How Does Air-Sea Wave Interaction Affect Tropical Cyclone Intensity? An Atmosphere-Wave-Ocean Coupled Model Study Based on Super Typhoon Mangkhut (2018). Earth and Space Science*, 9(3), p.e2021EA002136.

[20] Zed, A.A.A., Kansoh, R.M., Iskander, M.M. and Elkholy, M., (2022). *Wind and wave climate southeastern of the Mediterranean Sea based on a high-resolution SWAN model. Dynamics of Atmospheres and Oceans*, 99, p.101311.

[21] Booij, N.R.R.C., Ris, R.C. and Holthuijsen, L.H., (1999). *A third-generation wave model for coastal regions: 1. Model description and validation. Journal of geophysical research: Oceans*, 104(C4), p.7649-7666.

[22] Skamarock, W.C., Klemp, J.B. and Dudhia, J., (2005). *Coauthors, 2008: A description of the Advanced Research WRF version 3. NCAR Tech*, Note TN-4751STR.

[23] DHI (Danish Hydraulic Institute)., (2012). *MIKE 21 Spectral Wave Module. Scientific Documentation. Danish Hydraulic Institute*, p.66.

[24] Warner, J.C., Perlin, N. and Skyllingstad, E.D., (2008). *Using the Model Coupling Toolkit to couple earth system models. Environmental modelling & software*, 23(10-11), p.1240-1249.

[25] Ninomiya, J., Mori, N., Yasuda, T., Mase, H. and Kihara, N., (2012). *Improvement of Storm Surge Simulation Upon Parameterizations Of Coupled Air-Sea Interactions. Coastal Engineering Proceedings*, (33), p.51-51.

[26] Du, J., Larsén, X.G. and Bolaños, R., (2015). *A coupled atmospheric and wave modeling system for storm simulations. In Proceedings of EWEA Offshore 2015 conference European Wind Energy Association (EWEA).*

[27] Grifoll, M., Navarro, J., Pallares, E., Ràfols, L., Espino, M. and Palomares, A., (2016). *Ocean–atmosphere–wave characterisation of a wind jet (Ebro shelf, NW Mediterranean Sea). Nonlinear Processes in Geophysics*, 23(3), p.143-158.

[28] Ricchi, A., Miglietta, M.M., Falco, P.P., Benetazzo, A., Bonaldo, D., Bergamasco, A., Sclavo, M. and Carniel, S., (2016). *On the use of a coupled ocean–atmosphere–wave model during an extreme cold air outbreak over the Adriatic Sea. Atmospheric Research*, 172, p.48-65.

[29] Hoque, M.A., Perrie, W. and Solomon, S.M., (2020). *Application of SWAN model for storm generated wave simulation in the Canadian Beaufort Sea. Journal of Ocean Engineering and Science*, 5(1), p.19-34.

[30] Rusu, E. and Raileanu, A., (2016). *A multi-parameter data-assimilation approach for wave prediction in coastal areas. Journal of Operational Oceanography*, 9(1), p.13-25.

[31] Remya, P.G., Kumar, R. and Basu, S., (2014). *An assessment of wind forcing impact on a spectral wave model for the Indian Ocean. Journal of Earth System Science*, 123, p.1075-1087.

[32] SWAN team., (2018). *SWAN Scientific and Technical Documentation; Delft University of Technology: Delft, The Netherlands*, p.147.

[33] Ilia, A. and O'Donnell, J., (2018). *An assessment of two models of wave propagation in an estuary protected by breakwaters. Journal of Marine Science and Engineering*, 6(4), p.145.

[34] Strauss, D., Mirferendesk, H. and Tomlinson, R., (2007). *Comparison of two wave models for Gold Coast, Australia. Journal of Coastal Research*, p.312-316.

[35] Montoya, R.D., Arias, A.O., Royero, J.O. and Ocampo-Torres, F.J., (2013). *A wave parameters and directional spectrum analysis for extreme winds. Ocean Engineering*, 67, p.100-118.

[36] Fonseca, R.B., Gonçalves, M. and Guedes Soares, C., (2017). *Comparing the performance of spectral wave models for coastal areas. Journal of Coastal Research*, 33(2), p.331-346.

[37] Jacob, R., Larson, J. and Ong, E., (2005). *M× N communication and parallel interpolation in Community Climate System Model Version 3 using the model coupling toolkit. The International Journal of High Performance Computing Applications*, 19(3), p.293-307.

[38] Chotamonsak, C., Salathé Jr, E.P., Kreasuwan, J., Chantara, S. and Siriwitayakorn, K., (2011). *Projected climate change over Southeast Asia simulated using a WRF regional climate model. Atmospheric Science Letters*, 12(2), p.213-219.

[39] Soda, T., Shiotani, S., Makino, H. and Shimada, Y., (2017). *19. Research on Ship Navigation in Numerical Simulation of Weather and Ocean in a Bay. Navigational Systems and Simulators: Marine Navigation and Safety of Sea Transportation*, p.141.

[40] Osuri, K.K., Mohanty, U.C., Routray, A., Kulkarni, M.A. and Mohapatra, M., (2012). *Customization of WRF-ARW model with physical parameterization schemes for the simulation of tropical cyclones over North Indian Ocean. Natural Hazards*, 63, p.1337-1359.

[41] Srinivas, C.V., Hariprasad, D., Bhaskar Rao, D.V., Anjaneyulu, Y., Baskaran, R. and Venkatraman, B., (2013). *Simulation of the Indian summer monsoon regional climate using advanced research WRF model. International Journal of Climatology*, 33(5), p.1195-1210.

[42] Samala, B.K., Baerjee, S., Kaginalkar, A. and Dalvi, M., (2013). *Study of the Indian summer monsoon using WRF–ROMS regional coupled model simulations. Atmospheric Science Letters*, 14(1), p.20-27.

[43] Andraju, P., Kanth, A.L., Kumari, K.V. and Vijaya Bhaskara Rao, S., (2019). *Performance optimization of operational WRF model configured for Indian Monsoon Region. Earth Systems and Environment*, 3, p.231-239.

[44] Janjić, Z.I., (1994). *The step-mountain eta coordinate model: Further developments of the convection, viscous sublayer, and turbulence closure schemes. Monthly weather review*, 122(5), p.927-945.

[45] Hong, S.Y., Noh, Y. and Dudhia, J., (2006). *A new vertical diffusion package with an explicit treatment of entrainment processes. Monthly weather review*, 134(9), p.2318-2341.

[46] Fairall, C.W., Bradley, E.F., Hare, J.E., Grachev, A.A. and Edson, J.B., (2003). *Bulk parameterization of air–sea fluxes: Updates and verification for the COARE algorithm. Journal of climate*, 16(4), p.571-591.

[47] Taylor, P.K. and Yelland, M.J., (2001). *The dependence of sea surface roughness on the height and steepness of the waves. Journal of physical oceanography*, 31(2), p.572-590.

[48] Du, J., (2017). *Coupling atmospheric and ocean wave models for storm simulation.*

[49] Holthuijsen, L.H., (2010). *Waves in oceanic and coastal waters. Cambridge university press.*

[50] Hasselmann, K., (1974). *On the spectral dissipation of ocean waves due to white capping. Boundary-Layer Meteorology*, 6, p.107-127.

[51] Janssen, P.A., (1991). *Quasi-linear theory of wind-wave generation applied to wave forecasting. Journal of physical oceanography*, 21(11), p.1631-1642.

[52] Komen, G.J., Hasselmann, S. and Hasselmann, K., (1984). *On the existence of a fully developed wind-sea spectrum. Journal of physical oceanography*, 14(8), p.1271-1285.

[53] Hasselmann, K., Barnett, T.P., Bouws, E., Carlson, H., Cartwright, D.E., Enke, K., Ewing, J.A., Gienapp, A., Hasselmann, D.E., Kruseman, P. and Meerburg, A., (1973). *Measurements of wind-wave growth and swell decay during the Joint North Sea Wave Project (JONSWAP). Ergaenzungsheft zur Deutschen Hydrographischen Zeitschrift, Reihe A*.

[54] Collins, J.I., (1972). *Prediction of shallow-water spectra. Journal of Geophysical Research*, 77(15), p.2693-2707.

[55] Madsen, O.S., Poon, Y.K. and Graber, H.C., (1988). *Spectral wave attenuation by bottom friction: Theory. In Coastal engineering*, 1988, p.492-504.

[56] Komen, G.J., Cavaleri, L., Donelan, M., Hasselmann, K., Hasselmann, S. and Janssen, P.A.E.M. (1996). *Dynamics and modelling of ocean waves*, p. 554.

[57] Remya, P.G., Kumar, R., Basu, S. and Sarkar, A., (2012). *Wave hindcast experiments in the Indian Ocean using MIKE 21 SW model. Journal of earth system science*, 121, p.385-392.

[58] Sørensen, O.R., Kofoed-Hansen, H., Rugbjerg, M. and Sørensen, L.S., (2005). *A third-generation spectral wave model using an unstructured finite volume technique. In Coastal Engineering 2004: (In 4 Volumes)*, p.894-906.

[59] Soltanpour, M., Ranji, Z., Shibayama, T., Ghader, S. and Nishizaki, S., (2018). *Numerical simulation of tropical cyclones and storm surges in the Arabian Sea. Coastal Engineering Proceedings, (36),* p.1-11.

[60] Pakhirehzan, M., (2021). *Analysis of Ashobaa tropical cyclone-induced waves in the Northern Indian Ocean using coupled atmosphere–wave modeling. Marine Systems & Ocean Technology,* 16, p.124-141.

[61] Hong, S.Y., Dudhia, J. and Chen, S.H., (2004). *A revised approach to ice microphysical processes for the bulk parameterization of clouds and precipitation. Monthly weather review,* 132(1), p.103-120.

[62] Mlawer, E.J., Taubman, S.J., Brown, P.D., Iacono, M.J. and Clough, S.A., (1997). *Radiative transfer for inhomogeneous atmospheres: RRTM, a validated correlated-k model for the longwave. Journal of Geophysical Research: Atmospheres,* 102(D14), p.16663-16682.

[63] Dudhia, J., (1989). *Numerical study of convection observed during the winter monsoon experiment using a mesoscale two-dimensional model. Journal of Atmospheric Sciences,* 46(20), p.3077-3107.

[64] Nakanishi, M. and Niino, H., (2006). *An improved Mellor–Yamada level-3 model: Its numerical stability and application to a regional prediction of advection fog. Boundary-Layer Meteorology,* 119, p.397-407.

[65] Chen, F. and Dudhia, J., (2001). *Coupling an advanced land surface–hydrology model with the Penn State–NCAR MM5 modeling system. Part I: Model implementation and sensitivity. Monthly weather review,* 129(4), p.569-585.

[66] Pakhirehzan, M., Rahbani, M. and Malakooti, H., (2018). *Numerical Study of Winter Shamal Wind Forcing on the Surface Current and Wave Field in Bushehr's Offshore Using MIKE21. International Journal Of Coastal, Offshore And Environmental Engineering (ijcoe),* 3(2), p.57-65.